Journal of Computational Physics 258 (2014) 538–554

Contents lists available at ScienceDirect

Journal of Computational Physics

www.elsevier.com/locate/jcp

An efficient spectral method for computing dynamics of rotating two-component Bose–Einstein condensates via coordinate transformation

Ju Ming [a], Qinglin Tang [b], Yanzhi Zhang [c,*]

[a] Beijing Computational Science Research Center, No. 3 He-Qing Road, Hai-Dian District, Beijing 100084, PR China

[b] Department of Mathematics and Center for Computational Science and Engineering, National University of Singapore, 119076, Singapore

[c] Department of Mathematics and Statistics, Missouri University of Science and Technology, Rolla, MO 65409-0020, USA

ARTICLE INFO

Article history:
Received 22 May 2013
Received in revised form 11 October 2013
Accepted 23 October 2013
Available online 31 October 2013

Keywords:
Rotating two-component BECs
Coupled/vector Gross–Pitaevskii equations
Angular momentum rotation
Rotating Lagrangian coordinates
Time-splitting

ABSTRACT

In this paper, we propose an efficient and accurate numerical method for computing the dynamics of rotating two-component Bose–Einstein condensates (BECs) which is described by the coupled Gross–Pitaevskii equations (CGPEs) with an angular momentum rotation term and an external driving field. By introducing rotating Lagrangian coordinates, we eliminate the angular momentum rotation term from the CGPEs, which allows us to develop an efficient numerical method. Our method has spectral accuracy in all spatial dimensions and moreover it can be easily implemented in practice. To examine its performance, we compare our method with those reported in the literature. Numerical results show that to achieve the same accuracy, our method takes much shorter computing time. We also apply our method to study issues such as dynamics of vortex lattices and giant vortices in rotating two-component BECs. Furthermore, we generalize our method to solve the vector Gross–Pitaevskii equations (VGPEs) which is used to study rotating multi-component BECs.

1. Introduction

The Bose–Einstein condensation (BEC) affords an astonishing glimpse into the macroscopic quantum world and has been extensively studied since its first realization in 1995 [2,17]. Later, with the observation of quantized vortices in BECs [35,34], attention has been broaden to explore vortex states and their dynamics associated with superfluidity. Recently, rotating BECs which are known to exhibit highly regular vortex lattices have been heavily studied both experimentally and theoretically [1,33,30,20]. On the other hand, multi-component BECs admit numerous interesting phenomena absent from single-component condensates, for example, domain walls, vortons, square vortex lattices and so on; see [24,16,25–27] and references therein. As the simplest cases, two-component BECs provide a good opportunity to investigate the properties of multi-component condensation.

The first experiment of two-component BECs was carried out in $|F=2, m_f=2\rangle$ and $|F=1, m_f=-1\rangle$ hyperfine states of ^{87}Rb [36]. At temperatures T much smaller than the critical temperature T_c, a rotating two-component BEC with an external driving field (or an internal Josephson junction) can be well described by two self-consistent nonlinear Schrödinger

* Corresponding author.
E-mail addresses: jming@csrc.ac.cn (J. Ming), g0800880@nus.edu.sg (Q. Tang), zhangyanz@mst.edu (Y. Zhang).

0021-9991/$ – see front matter
http://dx.doi.org/10.1016/j.jcp.2013.10.044

equations (NLSEs), also known as the coupled Gross–Pitaevskii equations (CGPEs). The dimensionless CGPEs has the following form [26,40,45,5,20,7,27]:

$$i\frac{\partial \psi_1(\mathbf{x},t)}{\partial t} = \left[-\frac{1}{2}\nabla^2 + V_1(\mathbf{x}) + \left(\beta_{11}|\psi_1|^2 + \beta_{12}|\psi_2|^2\right) - \Omega L_z\right]\psi_1 - \lambda\psi_2, \tag{1.1}$$

$$i\frac{\partial \psi_2(\mathbf{x},t)}{\partial t} = \left[-\frac{1}{2}\nabla^2 + V_2(\mathbf{x}) + \left(\beta_{21}|\psi_1|^2 + \beta_{22}|\psi_2|^2\right) - \Omega L_z\right]\psi_2 - \lambda\psi_1, \quad \mathbf{x}\in\mathbb{R}^d,\ t>0. \tag{1.2}$$

Here, $\mathbf{x}\in\mathbb{R}^d$ ($d=2$ or 3) is the Cartesian coordinate vector, t is the time, and $\psi_j(\mathbf{x},t)$ is the complex-valued macroscopic wave function of the jth ($j=1,2$) component. The interaction constants $\beta_{jk}=\beta_{kj}=4\pi Na_{jk}/a_0$ (for $j,k=1,2$), where N is the total number of atoms in two-component BECs, a_0 is the spatial unit and $a_{jk}=a_{kj}$ represents the s-wave scattering lengths between the jth and kth components (positive for repulsive interaction and negative for attractive interaction). The constant λ describes the effective Rabi frequency to realize the internal atomic Josephson junction by a Raman transition, Ω represents the speed of angular momentum rotation and $L_z=-i(x\partial_y - y\partial_x)$ is the z-component of the angular momentum operator. The real-valued function $V_j(\mathbf{x})$ ($j=1,2$) represents the external trapping potential confining the jth component. In most BEC experiments, a harmonic potential is used, i.e.

$$V_j(\mathbf{x}) = \frac{1}{2}\begin{cases} \gamma_{x,j}^2x^2+\gamma_{y,j}^2y^2, & d=2,\\ \gamma_{x,j}^2x^2+\gamma_{y,j}^2y^2+\gamma_{z,j}^2z^2, & d=3, \end{cases} \qquad j=1,2. \tag{1.3}$$

The initial conditions of (1.1)–(1.2) are given by

$$\psi_j(\mathbf{x},0)=\psi_j^0(\mathbf{x}), \quad \mathbf{x}\in\mathbb{R}^d,\ j=1,2. \tag{1.4}$$

There are two important invariants associated with the CGPEs in (1.1)–(1.2): the *total mass* (*or normalization*), i.e.

$$N(t) := \left\|\Psi(\cdot,t)\right\|^2 = N_1(t)+N_2(t) \equiv \left\|\Psi(\cdot,0)\right\|^2 = 1, \quad t\geqslant 0, \tag{1.5}$$

where $\Psi(\mathbf{x},t)=(\psi_1(\mathbf{x},t),\psi_2(\mathbf{x},t))^T$ and $N_j(t)$ is the mass of the jth component at time $t\geqslant 0$, which is defined by

$$N_j(t) := \left\|\psi_j(\cdot,t)\right\|^2 = \int_{\mathbb{R}^d}\left|\psi_j(\mathbf{x},t)\right|^2 d\mathbf{x}, \quad t\geqslant 0,\ j=1,2, \tag{1.6}$$

and the *energy*

$$\begin{aligned} E(t)=E\big(\Psi(\cdot,t)\big) = \int_{\mathbb{R}^d}\Bigg[\sum_{j=1}^{2}\bigg(\frac{1}{2}|\nabla\psi_j|^2 + V_j(\mathbf{x})|\psi_j|^2 + \frac{\beta_{jj}}{2}|\psi_j|^4 - \Omega\,\mathrm{Re}\big(\psi_j^* L_z\psi_j\big)\bigg) \\ + \beta_{12}|\psi_1|^2|\psi_2|^2 - 2\lambda\,\mathrm{Re}\big(\psi_1\psi_2^*\big)\Bigg]d\mathbf{x} = E(0), \quad t\geqslant 0, \end{aligned} \tag{1.7}$$

where $\mathrm{Re}(f)$ and f^* represent the real part and the complex conjugate of a function f, respectively. In fact, if there is no external driving filed (i.e. $\lambda=0$ in (1.1)–(1.2)), the mass of each component is also conserved, i.e. $N_j(t)=N_j(0)$ ($j=1,2$) for $t\geqslant 0$. These invariants can be used, in particular, as benchmarks and validation of numerical algorithms for solving the CGPEs (1.1)–(1.2).

Many numerical methods have been proposed to study the dynamics of non-rotating single/multi-component BECs, i.e. when $\Omega=0$, with/without external driving field [5,8,14,37,28]. Among them, the time-splitting pseudo-spectral method in [5,14] is one of the most successful methods. It has spectral-order accuracy in space and can be easily implemented, i.e. it can achieve both the accuracy and efficiency. However, the appearance of the angular momentum rotational term hinders the direct application of those methods to study the rotating two-component BECs. Recently, several numerical methods were proposed for simulating the dynamics of rotating single/multi-component BECs [26,45,40,9,13,41,44,43]. For example, in [9,45], a pseudo-spectral type method was proposed by reformulating the problem in two-dimensional polar coordinates or three-dimensional cylindrical coordinates. While in [13,40], the authors introduced a time-splitting alternating direction implicit (TSADI) method, where the angular momentum rotation term is solved in x- and y-directions separately. Later, a generalized Laguerre–Fourier–Hermite pseudo-spectral method was proposed in [10]. These methods have higher spatial accuracy compared to those finite difference/element methods. However, the method in [9,45] has only the second- or fourth-order accuracy in the radial direction, while the implementation of the methods in [13,40,10] could be quite involved. One possible approach to overcome those limitations is to relax the constrain of the rotational term, which is the main aim of this paper. In this paper, we propose a simple and efficient numerical method to solve the CGPEs (1.1)–(1.2). The main merits of our method are: (i) Using a rotating Lagrangian coordinate transform, we reformulate the original CGPEs in (1.1)–(1.2) to one without angular momentum rotation term. Then, the time-splitting pseudo-spectral method designed

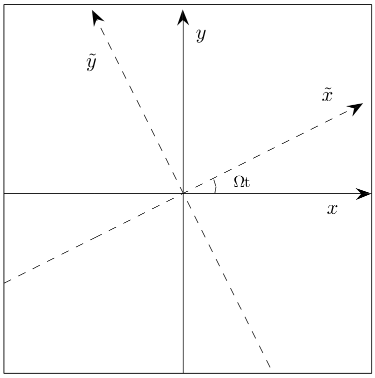

Fig. 1. Eulerian (or Cartesian) coordinates (x, y) (solid) and rotating Lagrangian coordinates $(\tilde{x}, \tilde{y})$ (dashed) in two dimensions for $\Omega > 0$ at a fixed time $t \geqslant 0$.

for the non-rotating BECs, which are of spectral order accuracy in space and easy to implemented, can be directly applied to solve the CGPEs in new coordinates. Moreover, (ii) our method solves the CGPEs in two splitting steps instead of three steps in the literature [45,40] and thus it is more efficient. In addition, the temporal accuracy of our method can be easily increased to higher order.

The paper is organized as follows. In Section 2, we introduce a rotating Lagrangian coordinate transform and cast the CGPEs (1.1)–(1.4) in the new coordinate system. A simple and efficient numerical method is introduced in Section 3 to discretize the CGPEs under rotating Lagrangian coordinates and it is subsequently generalized to solve the vector Gross–Pitaevskii equations (VGPEs) for multi-component BECs in Section 4. To test the performance of our method, in Section 5 we compare it with those reported in the literature and also apply it to study the dynamics of rotating two-component BECs. In Section 6, we make some concluding remarks.

2. CGPEs under rotating Lagrangian coordinates

In this section, we first introduce a rotating Lagrangian coordinate and then reformulate the CGPEs (1.1)–(1.4) in the new coordinate system. For any time $t \geqslant 0$, let $\mathbf{A}(t)$ be an orthogonal rotational matrix defined as [21,4,11]

$$\mathbf{A}(t) = \begin{pmatrix} \cos(\Omega t) & \sin(\Omega t) \\ -\sin(\Omega t) & \cos(\Omega t) \end{pmatrix}, \quad \text{if } d = 2, \tag{2.1}$$

and

$$\mathbf{A}(t) = \begin{pmatrix} \cos(\Omega t) & \sin(\Omega t) & 0 \\ -\sin(\Omega t) & \cos(\Omega t) & 0 \\ 0 & 0 & 1 \end{pmatrix}, \quad \text{if } d = 3. \tag{2.2}$$

It is easy to verify that $\mathbf{A}^{-1}(t) = \mathbf{A}^T(t)$ for any $t \geqslant 0$ and $\mathbf{A}(0) = \mathbf{I}$ with $\mathbf{I}$ the identity matrix. Referring the Cartesian coordinates $\mathbf{x}$ as the *Eulerian coordinates*, we introduce the *rotating Lagrangian coordinates* $\tilde{\mathbf{x}}$ as

$$\tilde{\mathbf{x}} = \mathbf{A}^{-1}(t)\mathbf{x} = \mathbf{A}^T(t)\mathbf{x} \quad \Longleftrightarrow \quad \mathbf{x} = \mathbf{A}(t)\tilde{\mathbf{x}}, \quad \mathbf{x} \in \mathbb{R}^d,\ t \geqslant 0. \tag{2.3}$$

Let $\phi_j(\tilde{\mathbf{x}}, t)$ denote the wave function in the new coordinates and

$$\phi_j(\tilde{\mathbf{x}}, t) := \psi_j(\mathbf{x}, t) = \psi_j\big(\mathbf{A}(t)\tilde{\mathbf{x}}, t\big), \quad \tilde{\mathbf{x}} \in \mathbb{R}^d,\ t \geqslant 0,\ j = 1, 2. \tag{2.4}$$

When $d = 3$, the transformation in (2.3) does not change the coordinates in z-direction (i.e. $\tilde{z} = z$), and thus the coordinate transformation essentially occurs only in xy-plane for $t > 0$. Fig. 1 depicts the geometrical relation between the xy-plane in the Eulerian coordinates and $\tilde{x}\tilde{y}$-plane in the rotating Lagrangian coordinates for any fixed time $t \geqslant 0$. In this paper, we assume that $\Omega \neq 0$. Furthermore, it is easy to see that when $t = 0$ the rotating Lagrangian coordinates $\tilde{\mathbf{x}}$ is exactly the same as the Eulerian coordinates $\mathbf{x}$, i.e. $\tilde{\mathbf{x}} \equiv \mathbf{x}$ when $t = 0$.

From (2.3)–(2.4), we obtain that

$$\partial_t\phi_j(\tilde{\mathbf{x}}, t) = \partial_t\psi_j(\mathbf{x}, t) + \nabla\psi_j(\mathbf{x}, t) \cdot \big(\dot{\mathbf{A}}(t)\tilde{\mathbf{x}}\big) = \partial_t\psi_j(\mathbf{x}, t) - \Omega(x\partial_y - y\partial_x)\psi_j(\mathbf{x}, t),$$
$$\nabla\phi_j(\tilde{\mathbf{x}}, t) = \mathbf{A}^{-1}(t)\nabla\psi_j(\mathbf{x}, t), \qquad \nabla^2\phi_j(\tilde{\mathbf{x}}, t) = \nabla^2\psi_j(\mathbf{x}, t), \quad \mathbf{x} \in \mathbb{R}^d,\ t \geqslant 0,\ j = 1, 2.$$

Substituting the above derivatives into (1.1)–(1.2) leads to the following d-dimensional CGPEs in the rotating Lagrangian coordinates $\tilde{\mathbf{x}}$:

$$i\frac{\partial\phi_1(\tilde{\mathbf{x}},t)}{\partial t}=\left[-\frac{1}{2}\nabla^2+W_1(\tilde{\mathbf{x}},t)+\left(\beta_{11}|\phi_1|^2+\beta_{12}|\phi_2|^2\right)\right]\phi_1-\lambda\phi_2, \tag{2.5}$$

$$i\frac{\partial\phi_2(\tilde{\mathbf{x}},t)}{\partial t}=\left[-\frac{1}{2}\nabla^2+W_2(\tilde{\mathbf{x}},t)+\left(\beta_{21}|\phi_1|^2+\beta_{22}|\phi_2|^2\right)\right]\phi_2-\lambda\phi_1,\quad \tilde{\mathbf{x}}\in\mathbb{R}^d,\ t>0. \tag{2.6}$$

The initial conditions of (2.5)–(2.6) are

$$\phi_j(\tilde{\mathbf{x}},0):=\phi_j^0(\tilde{\mathbf{x}})=\psi_j(\mathbf{x},0)=\psi_j^0(\mathbf{x}),\quad \tilde{\mathbf{x}}=\mathbf{x}\in\mathbb{R}^d. \tag{2.7}$$

In (2.5)–(2.6), $W_j(\tilde{\mathbf{x}},t)$ $(j=1,2)$ denotes the effective potential of the jth component, which is obtained from

$$W_j(\tilde{\mathbf{x}},t)=V_j\big(\mathbf{A}(t)\tilde{\mathbf{x}}\big),\quad \tilde{\mathbf{x}}\in\mathbb{R}^d,\ t\geqslant 0,\ j=1,2. \tag{2.8}$$

In particular, if $V_j(\mathbf{x})$ is a harmonic potential as defined in (1.3), then $W_j(\tilde{\mathbf{x}},t)$ has the form

$$W_j(\tilde{\mathbf{x}},t)=\frac{\gamma_{x,j}^2+\gamma_{y,j}^2}{4}\left(\tilde{x}^2+\tilde{y}^2\right)+\frac{\gamma_{x,j}^2-\gamma_{y,j}^2}{4}\left[\left(\tilde{x}^2-\tilde{y}^2\right)\cos(2\Omega t)+2\tilde{x}\tilde{y}\sin(2\Omega t)\right]+\begin{cases}0, & d=2,\\ \frac{1}{2}\gamma_{z,j}^2\tilde{z}^2, & d=3,\end{cases}$$

for $j=1,2$. Thus, when the external harmonic potentials are radially symmetric in two dimensions (2D) or cylindrically symmetric in three dimensions (3D), i.e. $\gamma_{x,j}=\gamma_{y,j}:=\gamma_{r,j}$, the potential

$$W_j(\tilde{\mathbf{x}},t)=V_j(\tilde{\mathbf{x}}),\quad \tilde{\mathbf{x}}\in\mathbb{R}^d,\ t\geqslant 0,\ j=1,2 \tag{2.9}$$

becomes time-independent.

In rotating Lagrangian coordinates, the wave functions $\Phi(\tilde{\mathbf{x}},t)=(\phi_1(\tilde{\mathbf{x}},t),\phi_2(\tilde{\mathbf{x}},t))^T$ satisfy the normalization

$$\widetilde{N}(t):=\left\|\Phi(\cdot,t)\right\|^2=\widetilde{N}_1(t)+\widetilde{N}_2(t)\equiv\left\|\Phi(\cdot,0)\right\|^2=1,\quad t\geqslant 0, \tag{2.10}$$

where $\widetilde{N}_j(t)$ defines the mass of the jth component at time $t\geqslant 0$, i.e.

$$\widetilde{N}_j(t):=\left\|\phi_j(\cdot,t)\right\|^2=\int_{\mathbb{R}^d}\left|\phi_j(\tilde{\mathbf{x}},t)\right|^2d\tilde{\mathbf{x}}=N_j(t),\quad t\geqslant 0,\ j=1,2. \tag{2.11}$$

When $\lambda=0$, the mass of each component is conserved, i.e. $\widetilde{N}_j(t)\equiv\widetilde{N}_j(0)$ for $t\geqslant 0$ and $j=1,2$. The energy associated with the CGPEs (2.5)–(2.6) is defined as

$$\begin{aligned}\widetilde{E}(t):=\widetilde{E}\big(\Phi(\cdot,t)\big)&=\int_{\mathbb{R}^d}\Bigg[\sum_{j=1}^{2}\left(\frac{1}{2}|\nabla\phi_j|^2+W_j(\tilde{\mathbf{x}},t)|\phi_j|^2-\int_0^t|\phi_j|^2\partial_\tau W_j(\tilde{\mathbf{x}},\tau)\,d\tau+\frac{\beta_{jj}}{2}|\phi_j|^4\right)\\&\qquad+\beta_{12}|\phi_1|^2|\phi_2|^2-2\lambda\,\mathrm{Re}\big(\phi_1\phi_2^*\big)\Bigg]d\tilde{\mathbf{x}}\\&=\widetilde{E}\big(\Phi(\cdot,0)\big)=E\big(\Psi(\cdot,0)\big)+\Omega\langle L_z\rangle(0)\\&=E\big(\Psi(\cdot,t)\big)+\Omega\langle L_z\rangle(0)\\&=E(t)+\Omega\langle L_z\rangle(0),\quad t\geqslant 0,\end{aligned} \tag{2.12}$$

where $\langle L_z\rangle(t)$ defined in (5.5) represents the total angular momentum expectation of a two-component BECs [45]. As we see in (2.9), when $\gamma_{x,j}=\gamma_{y,j}$ $(j=1,2)$, the potential $W_j(\tilde{\mathbf{x}},t)$ becomes time-independent, which leads to $\int_0^t|\phi_j|^2\partial_\tau W_j(\tilde{\mathbf{x}},\tau)\,d\tau\equiv 0$ in (2.12).

Compared to (1.1)–(1.2), the CGPEs (2.5)–(2.6) in rotating Lagrangian coordinates do not have the angular momentum rotational terms, which eliminates the main difficulties in discretizing the CGPEs using spectral method and allows us to develop an efficient method to solve (2.5)–(2.6).

3. Numerical method

In this section, we present a time-splitting sine pseudo-spectral method to study the dynamics of rotating two-component BECs. To the best of our knowledge, so far all numerical methods computing dynamics of rotating two-component BECs in the literature are based on discretizing the CGPEs (1.1)–(1.2) in Eulerian coordinates [5,45,40]. However, the appearance of rotating angular momentum terms in Eulerian coordinates makes it very challenging to develop an efficient method with high accuracy but low computational complexity. In the following, instead of simulating (1.1)–(1.2) in Eulerian coordinates, we solve the CGPEs (2.5)–(2.6) in rotating Lagrangian coordinates, which avoids the discretization of the angular momentum rotational term.

In practical simulations, we truncate the problem (2.5)–(2.6) into a bounded computational domain $\mathcal{D} \subset \mathbb{R}^d$ and consider

$$i\partial_t \phi_1(\tilde{\mathbf{x}},t) = \left[-\frac{1}{2}\nabla^2 + W_1(\tilde{\mathbf{x}},t) + \left(\beta_{11}|\phi_1|^2 + \beta_{12}|\phi_2|^2\right)\right]\phi_1 - \lambda\phi_2, \tag{3.1}$$

$$i\partial_t \phi_2(\tilde{\mathbf{x}},t) = \left[-\frac{1}{2}\nabla^2 + W_2(\tilde{\mathbf{x}},t) + \left(\beta_{21}|\phi_1|^2 + \beta_{22}|\phi_2|^2\right)\right]\phi_2 - \lambda\phi_1, \quad \tilde{\mathbf{x}} \in \mathcal{D},\ t > 0, \tag{3.2}$$

along with the initial conditions

$$\phi_j(\tilde{\mathbf{x}},t) = \phi_j^0(\tilde{\mathbf{x}}), \quad \tilde{\mathbf{x}} \in \overline{\mathcal{D}},\ j = 1,2, \quad \text{with} \int_{\overline{\mathcal{D}}} \left(\left|\phi_1^0(\tilde{\mathbf{x}})\right|^2 + \left|\phi_2^0(\tilde{\mathbf{x}})\right|^2\right) d\tilde{\mathbf{x}} = 1. \tag{3.3}$$

The following homogeneous Dirichlet boundary conditions are considered:

$$\phi_j(\tilde{\mathbf{x}},t) = 0, \quad \tilde{\mathbf{x}} \in \partial\mathcal{D},\ t \geqslant 0,\ j = 1,2. \tag{3.4}$$

Due to the confinement of the external potential $W_j(\mathbf{x},t)$ and the conservation of normalization (2.10) and energy (2.12), the wave function $\phi_j(\tilde{\mathbf{x}},t)$ vanishes as $|\tilde{\mathbf{x}}| \to \infty$. Hence, it is natural to consider homogeneous Dirichlet boundary conditions to the truncated problem (3.1)–(3.3). The use of more sophisticated boundary conditions for more generalized cases, e.g., in the absence of trapping potential, is an interesting topic that remains to be examined in the future [3,12]. Here, the computational domain $\mathcal{D} \subset \mathbb{R}^d$ is chosen as $\mathcal{D} = [a,b] \times [c,e]$ if $d = 2$ and $\mathcal{D} = [a,b] \times [c,e] \times [f,g]$ if $d = 3$. In practice, we use sufficiently large domain $\mathcal{D}$ to ensure the homogeneous Dirichlet boundary conditions do not introduce aliasing error. Usually, the diameter of the bounded computational domain depends on the problem. In general, it should be larger than the "Thomas–Fermi radius" [14,9].

3.1. Time-splitting method

In the following, we use the time-splitting method to discretize the problem (3.1)–(3.4) in time. To do it, we choose a time step $\Delta t > 0$ and define time sequence $t_n = n\Delta t$ for $n = 0,1,\ldots.$ Then from time $t = t_n$ to $t = t_{n+1}$, we numerically solve the CGPEs (3.1)–(3.2) in two steps, i.e. solving

$$i\partial_t \phi_j(\tilde{\mathbf{x}},t) = -\frac{1}{2}\nabla^2\phi_j(\tilde{\mathbf{x}},t) - \lambda\phi_{(3-j)}(\tilde{\mathbf{x}},t), \quad \tilde{\mathbf{x}} \in \mathcal{D},\ t_n \leqslant t \leqslant t_{n+1},\ j = 1,2, \tag{3.5}$$

and

$$i\partial_t \phi_j(\tilde{\mathbf{x}},t) = \left(W_j(\tilde{\mathbf{x}},t) + \sum_{k=1}^{2}\beta_{jk}|\phi_k|^2\right)\phi_j(\tilde{\mathbf{x}},t), \quad \tilde{\mathbf{x}} \in \mathcal{D},\ t_n \leqslant t \leqslant t_{n+1},\ j = 1,2. \tag{3.6}$$

In fact, Eq. (3.5) is the coupled linear Schrödinger equations and its discretization will be discussed later. Notice that in (3.6), both $|\phi_1(\tilde{\mathbf{x}},t)|$ and $|\phi_2(\tilde{\mathbf{x}},t)|$ are time invariants, i.e.

$$\left|\phi_j(\tilde{\mathbf{x}},t)\right| = \left|\phi_j(\tilde{\mathbf{x}},t_n)\right|, \quad \tilde{\mathbf{x}} \in \mathcal{D},\ t_n \leqslant t \leqslant t_{n+1},\ j = 1,2.$$

Thus, when $t \in [t_n, t_{n+1}]$, Eq. (3.6) reduces to

$$i\partial_t \phi_j(\tilde{\mathbf{x}},t) = \left(W_j(\tilde{\mathbf{x}},t) + \sum_{k=1}^{2}\beta_{jk}\left|\phi_k(\tilde{\mathbf{x}},t_n)\right|^2\right)\phi_j(\tilde{\mathbf{x}},t), \quad \tilde{\mathbf{x}} \in \mathcal{D},\ j = 1,2. \tag{3.7}$$

Integrating it exactly in time yields the solution of (3.6), i.e.

$$\phi_j(\tilde{\mathbf{x}},t) = \phi_j(\tilde{\mathbf{x}},t_n)\exp\left[-i\left((t-t_n)\sum_{k=1}^{2}\beta_{jk}\left|\phi_k(\tilde{\mathbf{x}},t_n)\right|^2 + \int_{t_n}^{t} W_j(\tilde{\mathbf{x}},\tau)\,d\tau\right)\right], \quad j = 1,2, \tag{3.8}$$

for $\tilde{\mathbf{x}} \in \mathcal{D}$ and $t \in [t_n, t_{n+1}]$.

Remark 3.1. If $V_j(\mathbf{x})$ $(j = 1, 2)$ is a harmonic potential as defined in (1.3), then the integral in (3.8) can be evaluated analytically, i.e.

$$\int_{t_n}^{t} W_j(\tilde{\mathbf{x}}, \tau)\, d\tau = \frac{(\gamma_{x,j}^2 + \gamma_{y,j}^2)(\tilde{x}^2 + \tilde{y}^2)}{4}(t - t_n) + U(\tilde{\mathbf{x}}, t) + \begin{cases} 0, & d = 2, \\ \frac{1}{2}\gamma_{z,j}^2 \tilde{z}^2 (t - t_n), & d = 3, \end{cases} \tag{3.9}$$

where

$$\begin{aligned} U(\tilde{\mathbf{x}}, t) &= \frac{(\gamma_{x,j}^2 - \gamma_{y,j}^2)}{4} \int_{t_n}^{t} \left[(\tilde{x}^2 - \tilde{y}^2)\cos(2\Omega\tau) + 2\tilde{x}\tilde{y}\sin(2\Omega\tau) \right] d\tau \\ &= \frac{(\gamma_{x,j}^2 - \gamma_{y,j}^2)}{8\Omega} \left[(\tilde{x}^2 - \tilde{y}^2)\big(\sin(2\Omega t) - \sin(2\Omega t_n)\big) - 2\tilde{x}\tilde{y}\big(\cos(2\Omega t) - \cos(2\Omega t_n)\big) \right]. \end{aligned}$$

Typically, when $\gamma_{x,j} = \gamma_{y,j}$ $(j = 1, 2)$, we have $U(\tilde{\mathbf{x}}, t) \equiv 0$.

For a general potential $V_j(\mathbf{x})$, if the integral in (3.8) cannot be found analytically, numerical quadratures such as Trapezoidal rule or Simpson's rule can be used to approximate it [9,11].

3.2. Discretization of coupled linear Schrödinger equations

In the following, we first introduce a linear transformation of the wave functions $\Phi(\tilde{\mathbf{x}}, t)$ to decouple the system of linear Schrödinger equations in (3.5) and then describe the sine pseudo-spectral discretization in two-dimensional cases. The generalization of it to three dimensions is straightforward. Let the matrix

$$\mathbf{P} = \begin{pmatrix} 1 & 1 \\ 1 & -1 \end{pmatrix}, \tag{3.10}$$

and denote

$$\begin{pmatrix} \varphi_1(\tilde{\mathbf{x}}, t) \\ \varphi_2(\tilde{\mathbf{x}}, t) \end{pmatrix} = \mathbf{P}\Phi(\tilde{\mathbf{x}}, t) = \begin{pmatrix} \phi_1(\tilde{\mathbf{x}}, t) + \phi_2(\tilde{\mathbf{x}}, t) \\ \phi_1(\tilde{\mathbf{x}}, t) - \phi_2(\tilde{\mathbf{x}}, t) \end{pmatrix}, \quad \tilde{\mathbf{x}} \in \mathbb{R}^d, \ t \geqslant 0. \tag{3.11}$$

Combining (3.5) and (3.11), we obtain the following equations for $\varphi_j(\tilde{\mathbf{x}}, t)$ $(j = 1, 2)$:

$$i\partial_t \varphi_1(\tilde{\mathbf{x}}, t) = -\frac{1}{2}\nabla^2 \varphi_1(\tilde{\mathbf{x}}, t) - \lambda\varphi_1(\tilde{\mathbf{x}}, t), \tag{3.12}$$

$$i\partial_t \varphi_2(\tilde{\mathbf{x}}, t) = -\frac{1}{2}\nabla^2 \varphi_2(\tilde{\mathbf{x}}, t) + \lambda\varphi_2(\tilde{\mathbf{x}}, t), \quad \tilde{\mathbf{x}} \in \mathcal{D}, \ t_n \leqslant t \leqslant t_{n+1}. \tag{3.13}$$

It is easy to see that the functions φ_1 and φ_2 are independent in (3.12)–(3.13), which allows us to solve them separately.

Choose two even integers $J, K > 0$ and denote the index set

$$\mathcal{T}_{JK} = \left\{ (p, q) \,\middle|\, 1 \leqslant p \leqslant J - 1, \ 1 \leqslant q \leqslant K - 1 \right\}. \tag{3.14}$$

Define the function

$$U_{pq}(\tilde{\mathbf{x}}) = \sin\big(\mu_p(\tilde{x} - a)\big)\sin\big(\nu_q(\tilde{y} - c)\big), \quad \tilde{\mathbf{x}} = (\tilde{x}, \tilde{y})^T \in \mathcal{D}, \ (p, q) \in \mathcal{T}_{JK}, \tag{3.15}$$

with

$$\mu_p = \frac{p\pi}{b - a}, \qquad \nu_q = \frac{q\pi}{e - c}, \quad (p, q) \in \mathcal{T}_{JK}.$$

Assume that

$$\varphi_j(\tilde{\mathbf{x}}, t) = \sum_{p=1}^{J-1}\sum_{q=1}^{K-1} \hat{\varphi}_{j,pq}(t) U_{pq}(\tilde{\mathbf{x}}), \quad \tilde{\mathbf{x}} \in \mathcal{D}, \ t \in [t_n, t_{n+1}], \ j = 1, 2, \tag{3.16}$$

where $\hat{\varphi}_{j,pq}(t)$ is the sine transform of $\varphi_j(\tilde{\mathbf{x}}, t)$ corresponding to frequencies (p, q). Substituting the ansatz (3.16) into (3.12)–(3.13) leads to

$$\hat{\varphi}_{1,pq}(t) = \hat{\varphi}_{1,pq}(t_n)\exp\left[-i\left(\frac{\mu_p^2 + \nu_q^2}{2} - \lambda \right)(t - t_n) \right], \tag{3.17}$$

$$\hat{\varphi}_{2,pq}(t) = \hat{\varphi}_{2,pq}(t_n)\exp\left[-i\left(\frac{\mu_p^2 + \nu_q^2}{2} + \lambda \right)(t - t_n) \right], \quad (p, q) \in \mathcal{T}_{JK}, \ t \in [t_n, t_{n+1}]. \tag{3.18}$$

Combining (3.17)–(3.18) and (3.16) and noticing the linear transformation in (3.11), we obtain a sine pseudo-spectral approximation to (3.5), i.e.

$$\phi_j(\tilde{\mathbf{x}},t)=\sum_{p=1}^{J-1}\sum_{q=1}^{K-1}\left[\cos\bigl(\lambda(t-t_n)\bigr)\hat{\phi}_{j,pq}(t_n)+i\sin\bigl(\lambda(t-t_n)\bigr)\hat{\phi}_{(3-j),pq}(t_n)\right]\eta_{pq}(t)U_{pq}(\tilde{\mathbf{x}}), \tag{3.19}$$

for $j=1,2$, where

$$\eta_{pq}(t)=\exp\left[-\frac{i}{2}\left(\mu_p^2+\nu_q^2\right)(t-t_n)\right],\quad (p,q)\in\mathcal{T}_{JK}.$$

In (3.19), $\hat{\phi}_{j,pq}(t)$ represents the sine transform of $\phi_j(\tilde{\mathbf{x}},t)$ $(j=1,2)$ corresponding to the frequencies (p,q). We remark here that although the solution (3.19) is found via (3.17)–(3.18), (3.16) and (3.11), in practice we only need to compute $\hat{\phi}_{1,pq}(t)$ and $\hat{\phi}_{2,pq}(t)$ to obtain (3.19).

3.3. Implementation of the method

For convenience of the readers, we will summarize our method and describe its implementation in this section. For simplicity of notations, the method will be presented only in two-dimensional cases, i.e. for $d=2$. Choose spatial mesh sizes $h_{\tilde{x}}=(b-a)/J$ and $h_{\tilde{y}}=(e-c)/K$ in $\tilde{x}$- and $\tilde{y}$-directions, respectively. Define

$$\tilde{x}_s=a+sh_{\tilde{x}},\quad 0\leqslant s\leqslant J,\qquad \tilde{y}_l=c+lh_{\tilde{y}},\quad 0\leqslant l\leqslant K. \tag{3.20}$$

Let $\phi_{j,sl}^n$ denote the numerical approximation of $\phi_j(\tilde{x}_s,\tilde{y}_l,t_n)$. From $t=t_n$ to $t=t_{n+1}$, we use the second-order Strang splitting method [39,22,14] to combine the two steps in (3.5) and (3.6), i.e.

$$\phi_{j,sl}^{(1)}=\phi_{j,sl}^n\exp\left[-i\left(\frac{\Delta t}{2}\sum_{k=1}^{2}\beta_{jk}\left|\phi_{k,sl}^n\right|^2+\int_{t_n}^{t+\Delta t/2}W_j(\tilde{x}_s,\tilde{y}_l,\tau)\,d\tau\right)\right], \tag{3.21}$$

$$\phi_{j,sl}^{(2)}=\sum_{p=1}^{J-1}\sum_{q=1}^{K-1}e^{-i\frac{\Delta t}{2}(\mu_p^2+\nu_q^2)}\left[\cos(\lambda\Delta t)\hat{\phi}_{j,pq}^{(1)}+i\sin(\lambda\Delta t)\hat{\phi}_{(3-j),pq}^{(1)}\right]\sin\left(\frac{sp\pi}{J}\right)\sin\left(\frac{lq\pi}{K}\right), \tag{3.22}$$

$$\phi_{j,sl}^{n+1}=\phi_{j,sl}^{(2)}\exp\left[-i\left(\frac{\Delta t}{2}\sum_{k=1}^{2}\beta_{jk}\left|\phi_{k,sl}^{(2)}\right|^2+\int_{t+\Delta t/2}^{t_{n+1}}W_j(\tilde{x}_s,\tilde{y}_l,\tau)\,d\tau\right)\right],\quad j=1,2, \tag{3.23}$$

for $1\leqslant s\leqslant J-1$, $1\leqslant l\leqslant K-1$ and $n=0,1,\ldots$. The discretization of boundary conditions in (3.4) leads to

$$\phi_{j,0l}^n=\phi_{j,s0}^n=0,\quad 0\leqslant s\leqslant J,\ 0\leqslant l\leqslant K,\ n=0,1,\ldots,\ j=1,2. \tag{3.24}$$

At time $t=0$, the initial conditions (3.3) are discretized as

$$\phi_{j,sl}^0=\phi_j^0(\tilde{x}_s,\tilde{y}_l),\quad 0\leqslant s\leqslant J,\ 0\leqslant l\leqslant K,\ j=1,2. \tag{3.25}$$

We remark here that if the potential $V_j(\mathbf{x})$ in (1.3) is replaced by a time-dependent potential, e.g., $V_j(\mathbf{x},t)$, the rotating Lagrangian coordinate transformation and the numerical method described in (3.21)–(3.25) are still valid provided that we replace $W_j(\tilde{\mathbf{x}},t)$ in (2.8) by $W_j(\tilde{\mathbf{x}},t)=V_j(\mathbf{A}(t)\tilde{\mathbf{x}},t)$ for $\tilde{\mathbf{x}}\in\mathbb{R}^d$ and $t\geqslant 0$.

Our method in (3.21)–(3.25) is explicit and it is easy to implement. It has spectral-order accuracy in space and the second order of accuracy in time. The temporal accuracy can be easily increased by using a high-order splitting schemes [39,22,14]. Furthermore, the memory cost is $O(JK)$ and the computational cost per time step is $O(JK\ln(JK))$ if the 2D CGPEs are solved. In 3D case, the memory and computational cost per time step are $O(JKL)$ and $O(JKL\ln(JKL))$, respectively, where $L>0$ is an even integer and $L+1$ represents the number of grid points in the z-direction.

Remark 3.2. The solutions obtained from (3.21)–(3.25) are grid functions on the bounded computational domain $\mathcal{D}$ in rotating Lagrangian coordinates. Usually, we need the wave functions $\psi_j(\mathbf{x},t_n)$ $(j=1,2)$ satisfying the CGPEs (1.1)–(1.2) over a set of fixed grid points in the Eulerian coordinates $\mathbf{x}$. To obtain them, we can use the standard Fourier/sine interpolation operators from the discrete numerical solutions of $\phi_j(\tilde{\mathbf{x}},t_n)$ $(j=1,2)$ to construct an interpolation continuous function over $\mathcal{D}$ and then use it to compute $\psi_j(\mathbf{x},t)$ over a set of fixed grid points in the Eulerian coordinates $\mathbf{x}$ [15,38]. The computational cost of transforming from $\phi_j(\tilde{\mathbf{x}},t)$ to $\psi_j(\mathbf{x},t)$ is $O(JK\ln(JK))$ by non-uniform fast Fourier/sine transform [18,19,23,29]. Note that this transformation is not necessary performed at every time step and it is carried out only when the values of $\psi_j(\mathbf{x},t)$ $(j=1,2)$ are needed. Thus, the total cost of the transformation process is low and will not affect the global cost of the method significantly. See Appendix A for more details.

4. Extension to rotating multi-component BECs

In Sections 2, 3, we present an efficient and accurate numerical method to compute the dynamics of rotating two-component BECs with an internal Josephson junction. In fact, this method can be easily generalized to solve the vector Gross–Pitaevskii equations (VGPEs) with an angular momentum rotation term and an external driving field, which is usually used to describe the dynamics of rotating multi-component BECs [5,32,30].

Suppose there are $M \geqslant 2$ species in multi-component BECs. Denote the complex-valued macroscopic wave function for the jth component as $\psi_j(\mathbf{x},t)$ for $j = 1,\dots,M$. Let $\Psi(\mathbf{x},t) = (\psi_1(\mathbf{x},t),\dots,\psi_M(\mathbf{x},t))^T$. Then the evolution of the wave function $\Psi(\mathbf{x},t)$ is governed by the following self-consistent VGPEs [5,32,30,31]:

$$i\frac{\partial \Psi(\mathbf{x},t)}{\partial t} = \left[-\frac{1}{2}\nabla^2 + \mathbf{V}(\mathbf{x}) + \mathbf{F}(\Psi) - \Omega L_z + g(t)\mathbf{B}\right]\Psi, \quad \mathbf{x}\in\mathbb{R}^d,\ t>0, \tag{4.1}$$

with the initial conditions

$$\Psi(\mathbf{x},0) = \Psi^0(\mathbf{x}) = \left(\psi_1^0(\mathbf{x}),\dots,\psi_M^0(\mathbf{x})\right)^T, \quad \mathbf{x}\in\mathbb{R}^d. \tag{4.2}$$

The matrix $\mathbf{V}(\mathbf{x}) = \mathrm{diag}(V_1(\mathbf{x}),\dots,V_M(\mathbf{x}))^T$ represents the external trapping potentials and $\mathbf{F}(\Psi) = \mathrm{diag}(F_1(\Psi),\dots,F_M(\Psi))^T$ with

$$F_j(\Psi) = \sum_{k=1}^{M}\beta_{jk}\left|\psi_k(\mathbf{x},t)\right|^2, \quad j=1,\dots,M,$$

where the constant β_{jk} describes the interaction strength between the jth and kth components. $g(t)$ is a real-valued scalar function and $\mathbf{B}$ is a real-valued diagonalizable constant matrix.

To solve (4.1)–(4.2), similarly we introduce the rotating Lagrangian coordinates as defined in (2.3)–(2.4) and cast the VGPEs in the new coordinates. Then we truncate it into a bounded computational domain $\mathcal{D}\subset\mathbb{R}^d$ and consider the following VGPEs for $\Phi(\tilde{\mathbf{x}},t) = (\phi_1(\tilde{\mathbf{x}},t),\dots,\phi_M(\tilde{\mathbf{x}},t))^T$:

$$i\frac{\partial \Phi(\tilde{\mathbf{x}},t)}{\partial t} = \left[-\frac{1}{2}\nabla^2 + \mathbf{W}(\tilde{\mathbf{x}},t) + \mathbf{F}(\Phi) + g(t)\mathbf{B}\right]\Phi, \quad \tilde{\mathbf{x}}\in\mathcal{D},\ t>0, \tag{4.3}$$

$$\Phi(\tilde{\mathbf{x}},0) = \left(\phi_1(\tilde{\mathbf{x}},0),\dots,\phi_M(\tilde{\mathbf{x}},0)\right)^T = \Psi(\tilde{\mathbf{x}},0), \quad \tilde{\mathbf{x}}\in\overline{\mathcal{D}}, \tag{4.4}$$

where $\mathbf{W}(\tilde{\mathbf{x}},t) = \mathrm{diag}(W_1(\tilde{\mathbf{x}},t),\dots,W_M(\tilde{\mathbf{x}},t))^T$ with $W_j(\tilde{\mathbf{x}},t) = V_j(\mathbf{A}(t)\tilde{\mathbf{x}})$ for $j=1,\dots,M$. The homogeneous Dirichlet boundary conditions are

$$\Phi(\tilde{\mathbf{x}},t) = 0, \quad \tilde{\mathbf{x}}\in\partial\mathcal{D},\ t>0. \tag{4.5}$$

From time $t=t_n$ to $t=t_{n+1}$, we split the VGPEs (4.3) into two subproblems and solve

$$i\partial_t\Phi(\tilde{\mathbf{x}},t) = \left[-\frac{1}{2}\nabla^2 + g(t)\mathbf{B}\right]\Phi, \quad \tilde{\mathbf{x}}\in\mathcal{D},\ t_n\leqslant t\leqslant t_{n+1}, \tag{4.6}$$

for a time step of length Δt, followed by solving

$$i\partial_t\Phi(\tilde{\mathbf{x}},t) = \left[\mathbf{W}(\tilde{\mathbf{x}},t) + \mathbf{F}(\Phi)\right]\Phi, \quad \tilde{\mathbf{x}}\in\mathcal{D},\ t_n\leqslant t\leqslant t_{n+1}, \tag{4.7}$$

for the same time step. Eq. (4.7) can be integrated exactly in time and the solution is

$$\phi_j(\tilde{\mathbf{x}},t) = \phi_j(\tilde{\mathbf{x}},t_n)\exp\left[-i\left((t-t_n)F_j\left(\Phi(\tilde{\mathbf{x}},t_n)\right) + \int_{t_n}^{t}W_j(\tilde{\mathbf{x}},\tau)\,d\tau\right)\right], \quad j=1,\dots,M, \tag{4.8}$$

for $\tilde{\mathbf{x}}\in\mathcal{D}$ and $t\in[t_n,t_{n+1}]$.

On the other hand, since $\mathbf{B}$ is a diagonalizable matrix, there exists a matrix $\mathbf{D}$ and a diagonal matrix $\mathbf{\Lambda} = \mathrm{diag}(\lambda_1,\dots,\lambda_M)$ such that $\mathbf{B} = \mathbf{D}^{-1}\mathbf{\Lambda}\mathbf{D}$. Denote

$$\Upsilon(\tilde{\mathbf{x}},t) := \mathbf{D}\Phi(\tilde{\mathbf{x}},t) = \left(\varphi_1(\tilde{\mathbf{x}},t),\dots,\varphi_M(\tilde{\mathbf{x}},t)\right)^T. \tag{4.9}$$

Then from (4.6), we obtain

$$i\partial_t\Upsilon(\tilde{\mathbf{x}},t) = \left[-\frac{1}{2}\nabla^2 + g(t)\mathbf{\Lambda}\right]\Upsilon, \quad \tilde{\mathbf{x}}\in\mathcal{D},\ t_n\leqslant t\leqslant t_{n+1}. \tag{4.10}$$

Again we will only present the discretization in 2D case and the generalization to 3D is straightforward. Discretizing (4.10) by sine pseudo-spectral method and noticing $\Phi = \mathbf{D}^{-1}\Upsilon$, we obtain the solution of (4.6) as

$$\Phi(\tilde{\mathbf{x}},t) = \left(\mathbf{D}^{-1} e^{-i\Lambda \int_{t_n}^{t} g(\tau)\,d\tau}\right) \sum_{p=1}^{J-1} \sum_{q=1}^{K-1} e^{-\frac{i}{2}(\mu_p^2+\mu_q^2)(t-t_n)} \left(\mathbf{D}\widehat{\Phi}_{pq}(t_n)\right) U_{pq}(\tilde{\mathbf{x}}), \tag{4.11}$$

for $\tilde{\mathbf{x}} \in \mathcal{D}$ and $t \in [t_n, t_{n+1}]$, where $\widehat{\Phi}_{pq}(t_n) = (\hat{\phi}_{1,pq}(t_n), \ldots, \hat{\phi}_{M,pq}(t_n))^T$ with $\hat{\phi}_{j,pq}(t_n)$ $(1 \leqslant j \leqslant M)$ the discrete sine transform of $\phi_j(\tilde{\mathbf{x}}, t_n)$ corresponding to the frequency (p,q). Similarly, we can use the second-order Strange splitting method to combine the above two steps and it can be easily implemented by replacing (3.21) and (3.23) by (4.8) and (3.22) by (4.11).

5. Numerical results

In this section, we first test the accuracy of our method presented in Section 3 and compare its accuracy and efficiency with the method reported in [40]. Then we apply our method to study the dynamics of vortex lattices and other properties of rotating two-component BECs.

5.1. Comparison of methods

In this section, we test the accuracy and efficiency of our method and compare it with the time-splitting alternating direction implicit (TSADI) method proposed in [40]. The TSADI method has spectral-order accuracy in all spatial directions and thus it is more accurate than other methods in the literature. We solve the two-dimensional (i.e. $d=2$) CGPEs with the parameters $\Omega = 0.4$, $\lambda = 1.0$, $\gamma_{x,j} = \gamma_{y,j} = 1$ (for $j = 1, 2$), and

$$\begin{pmatrix} \beta_{11} & \beta_{12} \\ \beta_{21} & \beta_{22} \end{pmatrix} = 50 \begin{pmatrix} 1.03 & 1.0 \\ 1.0 & 0.97 \end{pmatrix}.$$

The initial conditions are chosen as

$$\psi_1^0(\mathbf{x}) = \frac{1}{\sqrt{2\pi}} e^{-\frac{x^2+y^2}{2}}, \qquad \psi_2^0(\mathbf{x}) = \frac{1.5^{1/4}}{\sqrt{2\pi}} e^{-\frac{x^2+1.5y^2}{2}}, \quad \mathbf{x} \in \mathbb{R}^2. \tag{5.1}$$

We remark here that the TSADI method in [40] is different from our method mainly in three aspects: (i) The TSADI method solves the CGPEs (1.1)–(1.2) in Eulerian coordinates, while our method solves the CGPEs (2.5)–(2.6) in rotating Lagrangian coordinates. (ii) To decouple the nonlinearity and internal Josephson junction terms, the TSADI method splits the CGPEs into three steps, while our method solves the problem in new coordinates in two steps. (iii) In [40], the angular momentum rotational term $-\Omega L_z \psi$ is "split" into d parts (for $d = 2$ or 3) using the ADI method. In contrast, in our method we use coordinate transformation to eliminate this term and thus avoid to discretize it. For details of the TSADI method, we refer readers to [13,40].[1]

Since the TSADI and our methods solve the problem in different coordinates, to compare them in a fair way we will use the same spatial mesh size and time step. In our simulations, we choose sufficiently large computational domain $\mathcal{D} = [-16, 16]^2$ for both methods. Denote $\phi_j^{(h_{\tilde{x}}, h_{\tilde{y}}, k)}(t)$ as the numerical approximation of $\phi_j(\tilde{\mathbf{x}}, t)$, which is obtained by using our method with time step k and spatial mesh size $h_{\tilde{x}}$ and $h_{\tilde{y}}$. Similarly, let $\psi_j^{(h_x, h_y, k)}(t)$ be the numerical solution of $\psi_j(\mathbf{x}, t)$ from the TSADI method. Here we take $h_x = h_y = h_{\tilde{x}} = h_{\tilde{y}} := h$. With a slight abuse of notation, we let $\phi_j(t)$ (or $\psi_j(t)$) represent the numerical solution with very fine mesh size $h = 1/64$ and small time step $k = 0.0001$ and assume it to be sufficiently good representation of the exact solution at time t. Tables 1, 2 show the spatial and temporal errors of two methods, where the errors are computed by

$$\left\| \Phi(t) - \Phi^{(h,h,k)}(t) \right\|_{l^2} = \sqrt{\sum_{j=1}^{2} \left\| \phi_j(t) - \phi_j^{(h,h,k)}(t) \right\|_{l^2}^2}$$

for our method and $\|\Psi(t) - \Psi^{(h,h,k)}(t)\|_{l^2}$ for the TSADI method. In addition, we present the CPU time consumed by each method in solving the problem from time $t = 0$ to $t = 2$. To calculate the spatial errors in Table 1, we always use a very small time step $k = 0.0001$ so that the errors from time discretization can be neglected compared to those from spatial discretization. On the other hand, in Table 2, we always use $h = 1/64$ which is the same as those used in obtaining the 'exact' solution, so that one can regard the spatial discretization as 'exact' and the only errors are from time discretization.

[1] See Eq. (3.14) in [40] for more details of the TSADI method. Notice that in (3.14) $\psi_{1,jk}^{(3)}$, $\psi_{2,jk}^{(3)}$, $\psi_{1,jk}^{(5)}$ and $\psi_{2,jk}^{(5)}$ are mistyped. For example, $\psi_{1,jk}^{(3)}$ and $\psi_{2,jk}^{(3)}$ should be computed as [45,6]

$$\psi_{1,jk}^{(3)} = \cos(\lambda\Delta t/2)\psi_{1,jk}^{(2)} + i\sin(\lambda\Delta t/2)\psi_{2,jk}^{(2)}, \tag{5.2}$$

$$\psi_{2,jk}^{(3)} = \cos(\lambda\Delta t/2)\psi_{2,jk}^{(2)} + i\sin(\lambda\Delta t/2)\psi_{1,jk}^{(2)}. \tag{5.3}$$

Similarly, $\psi_{1,jk}^{(5)}$ and $\psi_{2,jk}^{(5)}$ should also be changed correspondingly.

Table 1
Spatial discretization errors at time $t = 2$ and the computing time (i.e., CPU time in second) spent by each method, where the time step $k = 0.0001$ is used in both methods.

Mesh size h	TSADI method		Our method	
	Error	Computing time (sec.)	Error	Computing time (sec.)
1	0.8562	19.50	0.9408	13.16
1/2	0.1202	81.19	0.1202	53.09
1/4	6.9425E−4	383.74	6.8771E−4	235.54
1/8	1.1267E−7	1627.15	3.8578E−8	1002.43
1/16	< 1.0E−8	7450.26	< 1.0E−8	4502.41

Table 2
Temporal discretization errors at time $t = 2$ and the computing time (i.e., CPU time in second) spent by each method, where the mesh size $h = 1/64$ is used in both methods.

Time step k	TSADI method		Our method	
	Error	Computing time (sec.)	Error	Computing time (sec.)
1/40	1.7511E−2	649.14	1.0164E−2	415.21
1/80	4.3444E−3	1277.80	2.5310E−3	817.31
1/160	1.0839E−3	2587.39	6.3204E−4	1620.82
1/320	2.7064E−4	5033.16	1.5785E−4	3207.06
1/640	6.7444E−5	9956.51	3.9339E−5	6383.44

From Tables 1, 2, we see that both the TSADI method and our method have the spectral-order accuracy in space and the second-order accuracy in time. However, for the same numerical parameters (i.e. h and k), the TSADI method is much slower than our method. Usually, the computing time spent by the TSADI method is around 1.5 times more than that taken by our method. For example, when $h = 1/64$ and $k = 1/640$, the computing time by the TSADI method is 9956.51 seconds and our method only needs 6383.44 seconds. This is mainly caused by two factors: (i) In [40], the CGPEs is solved by three splitting steps, i.e. there is an extra step of $i\partial_t\psi_j = -\lambda\psi_{(3-j)}$ (for $j = 1, 2$) to solve at each time step. However, we notice that the term $-\lambda\psi_{(3-j)}$ can be combined with $\nabla^2\psi_j$ by a linear transformation of the wave functions, which avoids introducing an extra step to solve the internal Josephson junction terms. Hence, our method is more efficient especially in higher dimensions or when more components are involved. (ii) The TSADI method splits the spatial operator into the operators in x- and y-directions. Equivalently, it discretizes the x- and y-direction separately. While our method treats all spatial directions simultaneously, which saves the time in doing discrete sine transform. Furthermore, we remark here that the temporal accuracy of our method can be easily increased to higher order by using high-order time-splitting methods [39,42,14], while the improvement of the temporal accuracy of the TSADI method is not trivial.

The computing time of both methods increases when smaller time step or spatial mesh size are used. Especially, for a fixed time step k, if the mesh size h decreases by a factor α_h, then the time spent by both methods increases by a factor of α_h^2. While for fixed mesh size h, if the time step k decreases by a factor α_k, then the time spent by both methods increases by a factor of α_k. We remark here that our motivation is to compare the speed of two methods and thus their computer programs are run on the same computer. We understand that the computing time presented in Tables 1, 2 can be shorten if one uses an advanced computer or does parallel computations, which however is not our interest here.

In addition, we study the conservation of energy and total mass. Fig. 2 shows the time evolution of the energy and total mass for time $t \in [0, 10]$, where the mesh size $h = 1/16$ and time step $k = 0.0001$. It shows that both the TSADI and our methods numerically conserve the total mass and energy, but our method has a better conservation in energy (cf. Fig. 2 left). In fact, it can prove that our method conserves the total mass in the discrete level, but the energy is not exactly conserved in our method.

To further test our method, in Sections 5.2, 5.3 we will apply it to study the dynamical properties of rotating two-component BECs, e.g., dynamics of mass, angular momentum expectation and condensate widths. Our numerical results will be compared with those reported in [45]. In [45], a numerical method was proposed for simulating dynamics of rotating two-component BECs, in which the polar coordinates or cylindrical coordinates were used to resolve the difficulty caused by the angular momentum rotational term and a second- or fourth-order finite difference/element discretion is used in the radial direction. Thus, it has low-order accuracy in the radial direction.

5.2. Dynamics of the mass

We study dynamics of the mass of each component, i.e. $N_j(t) = \|\psi_j(\cdot,t)\|^2$ for $j = 1, 2$, and also the total mass $N(t) = N_1(t) + N_2(t)$. In our simulations, we solve two-dimensional CGPEs with the following parameters: $\lambda = 1$, $\Omega = 0.6$ and two-dimensional harmonic potentials are considered with $\gamma_{x,j} = \gamma_{y,j} = 1$ $(j = 1, 2)$. The initial conditions are chosen as

$$\psi_1^0(\mathbf{x}) = \frac{x + iy}{\sqrt{\pi}} \exp\left(-\frac{x^2 + y^2}{2}\right), \qquad \psi_2^0(\mathbf{x}) = 0, \quad \mathbf{x} \in \mathbb{R}^2.$$

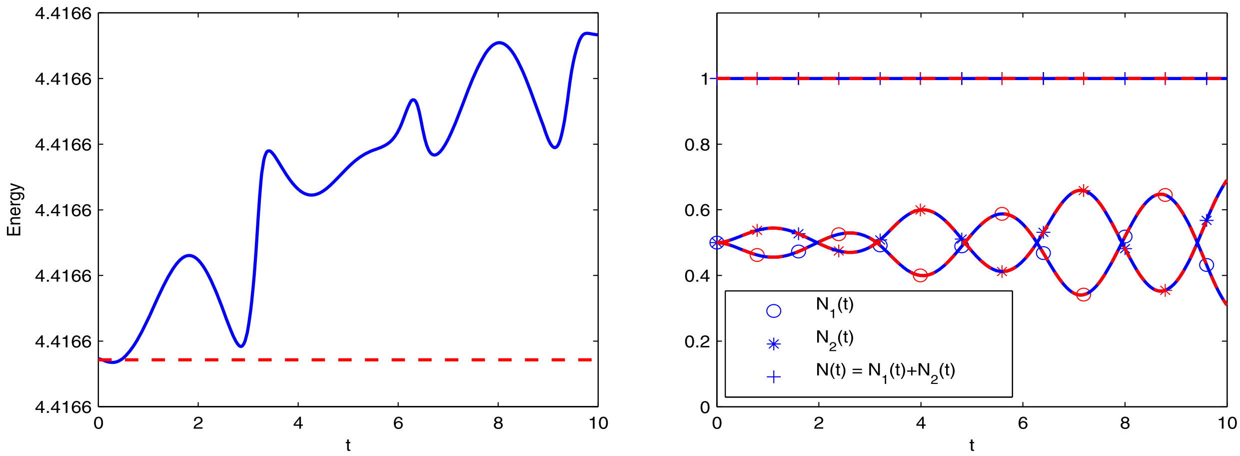

Fig. 2. Dynamics of the energy and the total mass for $t = [0, 10]$, where the mesh size $h = 1/16$ and time step $k = 0.0001$. Solid blue line: computed from TSADI method; dash red line: obtained from our method. (For interpretation of the references to color in this figure legend, the reader is referred to the web version of this article.)

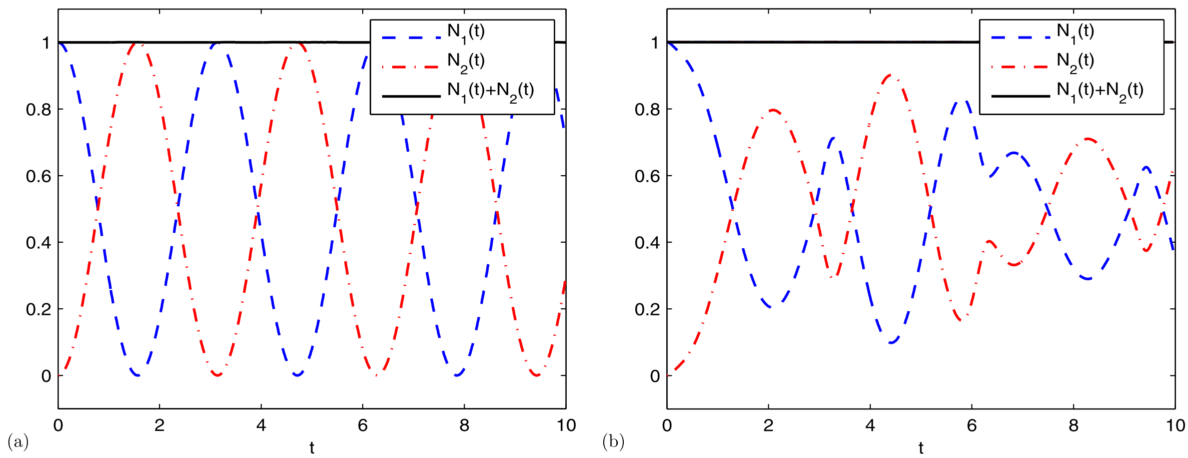

Fig. 3. Time evolution of the mass $N_j(t) = \|\psi_j(\cdot, t)\|^2$ $(j = 1, 2)$ and $N(t) = N_1(t) + N_2(t)$ for two sets of interaction parameters: (a) $\beta_{11} = \beta_{12} = \beta_{22} = 500$; (b) $\beta_{11} = 500$, $\beta_{22} = 400$, $\beta_{12} = \beta_{21} = 300$.

That is, initially all atoms are in the first component. Then we study the dynamics with respect to the following two sets of parameters:

$$\text{(i)} \quad \begin{pmatrix} \beta_{11} & \beta_{12} \\ \beta_{21} & \beta_{22} \end{pmatrix} = 500 \begin{pmatrix} 1.0 & 1.0 \\ 1.0 & 1.0 \end{pmatrix}; \qquad \text{(ii)} \quad \begin{pmatrix} \beta_{11} & \beta_{12} \\ \beta_{21} & \beta_{22} \end{pmatrix} = 500 \begin{pmatrix} 1.0 & 0.6 \\ 0.6 & 0.8 \end{pmatrix}. \tag{5.4}$$

This is one example studied in [45]. We remark here that our goal is to test the performance of our method by comparing it with the available method, and thus we use the same example as that in [45] for the purpose of easy comparison.

In our simulations, the computational domain is chosen as $\mathcal{D} = [-8, 8]^2$. We use mesh size $h_{\tilde{x}} = h_{\tilde{y}} = \frac{1}{32}$ and time step $\Delta t = 0.0001$. Fig. 3 shows the time evolution of $N_1(t)$, $N_2(t)$ and $N(t)$ for time $t \in [0, 10]$. From it, we see that when $\beta_{11} = \beta_{12} = \beta_{22}$ (cf. Fig. 3(a)), the two components exchange their mass periodically with period $T = \pi/\lambda = \pi$. While when $\beta_{11} \neq \beta_{12} \neq \beta_{22}$, $N_1(t)$ and $N_2(t)$ are not periodical functions (cf. Fig. 3(b)). In both cases, the total mass $N(t) = N_1(t) + N_2(t)$ is always conserved. The above observations are consistent with the analytical results reported in [45, 6]. Moreover, our numerical results in Fig. 3 are the same as those obtained in [45][2] where a numerical method based on Eulerian coordinates was used. However, our extensive simulations show that the computing time taken by our method is much shorter than that by the method in [45], if the same accuracy is required.

[2] See Fig. 3 in [45].

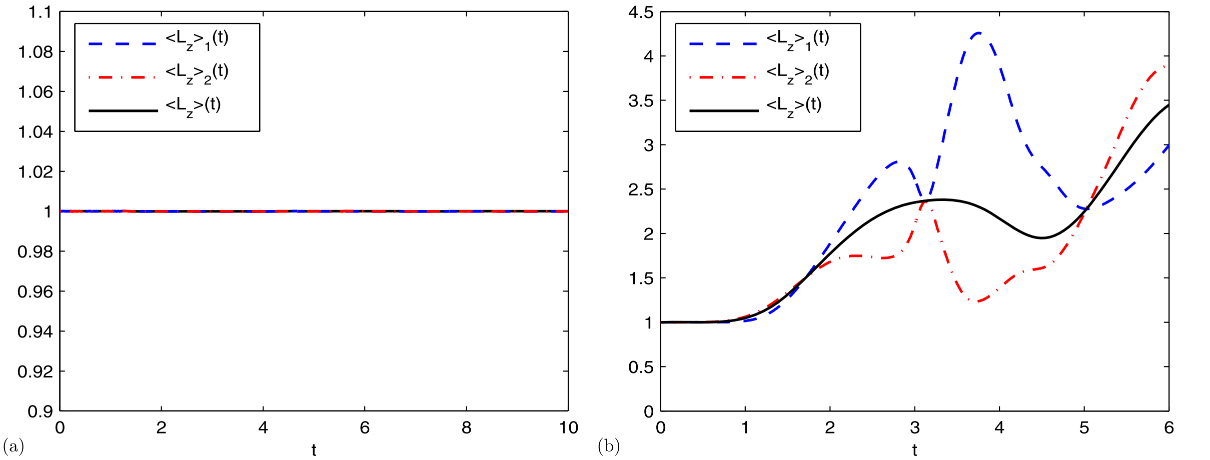

Fig. 4. Time evolution of angular momentum expectation $\langle L_z\rangle_j(t)$ $(j=1,2)$ and $\langle L_z\rangle(t)$ for two sets of trapping frequencies: (a) $\gamma_{x,j}=\gamma_{y,j}=1$ $(j=1,2)$; (b) $\gamma_{x,1}=\gamma_{y,1}=1$, $\gamma_{x,2}=1.05$, $\gamma_{y,2}=0.9$.

5.3. Dynamics of angular momentum expectation and condensate widths

There are two important quantities in describing the dynamics of rotating two-component BECs: angular momentum expectation and condensate widths. In the following, we numerically study their dynamics using our method described in Section 3. For convenience of the readers, we first review the definition of these two quantities; see more details in [9,45,40,5,11]. The total angular momentum expectation of two-component BECs is defined as

$$\langle L_z\rangle(t)=\sum_{j=1}^{2}\int_{\mathbb{R}^d}\psi_j^*(\mathbf{x},t)L_z\psi_j(\mathbf{x},t)\,d\mathbf{x},\quad t\geqslant 0, \tag{5.5}$$

and the angular momentum expectation of the jth component is

$$\langle L_z\rangle_j(t)=\frac{1}{N_j(t)}\int_{\mathbb{R}^d}\psi_j^*(\mathbf{x},t)L_z\psi_j(\mathbf{x},t)\,d\mathbf{x},\quad t\geqslant 0,\ j=1,2. \tag{5.6}$$

Usually, the angular momentum expectation can be used to measure the vortex flux. The condensate width of two-component BECs in the α-direction ($\alpha=x$, y or z) is defined as

$$\sigma_\alpha=\sqrt{\delta_\alpha(t)}=\sqrt{\delta_{\alpha,1}(t)+\delta_{\alpha,2}(t)},\quad t\geqslant 0,\ \alpha=x,\,y\text{ or }z, \tag{5.7}$$

where

$$\delta_{\alpha,j}(t)=\langle\alpha^2\rangle_j(t)=\int_{\mathbb{R}^d}\alpha^2\left|\psi_j(\mathbf{x},t)\right|^2d\mathbf{x},\quad t\geqslant 0,\ j=1,2. \tag{5.8}$$

To study the dynamics of angular momentum expectation and condensate widths, we choose the following parameters in the CGPEs (3.1)–(3.2): $d=2$, $\Omega=0.6$, $\lambda=1$ and

$$\begin{pmatrix}\beta_{11} & \beta_{12}\\ \beta_{21} & \beta_{22}\end{pmatrix}=400\begin{pmatrix}1.0 & 0.97\\ 0.97 & 0.94\end{pmatrix}. \tag{5.9}$$

The initial conditions are taken as

$$\psi_j^0(\mathbf{x})=\frac{x+iy}{\sqrt{2\pi}}\exp\left(-\frac{x^2+y^2}{2}\right),\quad \mathbf{x}\in\mathbb{R}^2,\ j=1,2.$$

The computational domain is chosen as $\mathcal{D}=[-24,24]^2$ with the mesh size $h_{\tilde{x}}=h_{\tilde{y}}=\frac{3}{64}$ and time step is $k=0.0001$.

Fig. 4 presents the dynamics of angular momentum expectations for two sets of trapping frequencies: (i) $\gamma_{x,1}=\gamma_{y,1}=\gamma_{x,2}=\gamma_{y,2}=1$; (ii) $\gamma_{x,1}=\gamma_{y,1}=1$, $\gamma_{x,2}=1.05$, $\gamma_{y,2}=0.9$. It shows that the total angular momentum expectation $\langle L_z\rangle(t)$ is conserved as long as both external trapping potentials $V_1(\mathbf{x})$ and $V_2(\mathbf{x})$ in (1.3) are symmetric (cf. Fig. 4(a)). While when $\lambda\neq 0$, if at least one of the external potentials is asymmetric, none of $\langle L_z\rangle_1(t)$, $\langle L_z\rangle_2(t)$ and $\langle L_z\rangle(t)$ is conserved (cf. Fig. 4(b)).

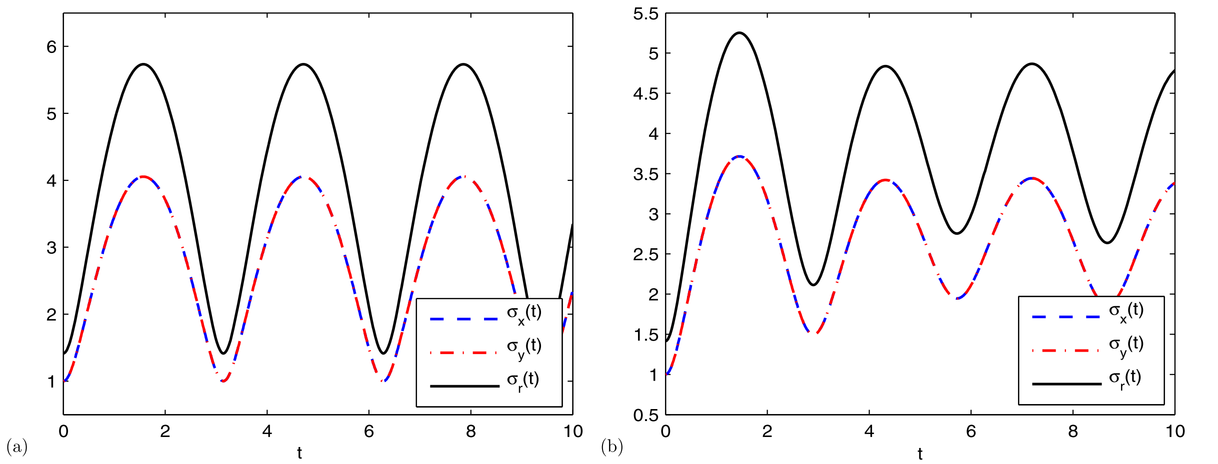

Fig. 5. Time evolution of condensate widths $\sigma_x(t)$, $\sigma_y(t)$ and $\sigma_r(t)$ for two sets of trapping frequencies: (a) $\gamma_{x,j}=\gamma_{y,j}=1$ $(j=1,2)$; (b) $\gamma_{x,1}=\gamma_{y,1}=1$, $\gamma_{x,2}=\gamma_{y,2}=1.2$.

In addition, the results in Fig. 4 are the same as those reported in [45][3] but the computing time used by our method is much less.

Fig. 5 shows the dynamics of condensate widths for $\sigma_x(t)$, $\sigma_y(t)$ and $\sigma_r(t):=\sqrt{\sigma_x^2(t)+\sigma_y^2(t)}$ for two sets of trapping frequencies: (i) $\gamma_{x,1}=\gamma_{y,1}=\gamma_{x,2}=\gamma_{y,2}:=\gamma=1$; (ii) $\gamma_{x,1}=\gamma_{y,1}=1$, $\gamma_{x,2}=\gamma_{y,2}=1.2$. From it, we see that when the two components have the same external trapping potentials, the condensate widths $\sigma_x(t)$, $\sigma_y(t)$ and $\sigma_r(t)$ are periodic functions with period $T=\pi/\gamma=\pi$ (cf. Fig. 5(a)). If the potential $V_1(\mathbf{x})\neq V_2(\mathbf{x})$ in (1.3), the condensate widths are not periodic functions. The above results are consistent with those observed in [45].[4]

5.4. Dynamics of vortex lattices in slowly rotating condensates

In this section, we apply our method to study the dynamics of vortex lattices in slowly rotating two-component BECs, i.e. when Ω is small. The initial data are taken as the stationary vortex lattices, which are computed by choosing $\Omega=0.9$, $\lambda=0$, $\gamma_{x,j}=\gamma_{y,j}=1$ $(j=1,2)$ in the harmonic potential (1.3) and

$$\begin{pmatrix}\beta_{11} & \beta_{12}\\ \beta_{21} & \beta_{22}\end{pmatrix}=500\begin{pmatrix}1.0 & -0.25\\ -0.25 & 1.0\end{pmatrix}.$$

Due to the attractive interaction between two components, i.e. $\beta_{12}=\beta_{21}<0$, initially the stationary vortex lattices of two components are exactly the same. Then at time $t=0$,

Case (i) Change the symmetric external potentials to asymmetric by setting $\gamma_{x,1}=\gamma_{y,2}=1.05$ and $\gamma_{x,2}=\gamma_{y,1}=0.95$;
Case (ii) Turn on the external driving field by setting $\lambda=1$.

The computational domain is chosen as $\mathcal{D}=[-24,24]^2$ with mesh size $h_{\tilde{x}}=h_{\tilde{y}}=\frac{3}{32}$ and time step $k=0.0001$.

Figs. 6, 7 show the contour plots of $|\psi_1|$ and $|\psi_2|$ at different time t in Cases (i) and (ii), respectively, where the displayed domain is $(x,y)\in[-10,10]^2$. At time $t=0$, the vortex lattices of two components are identical and there are 19 vortices in each lattice. In Case (i), the lattices rotate periodically due to the anisotropy of the external potentials and the number of vortices is conserved during the dynamics (cf. Fig. 6). While in Fig. 7, we see that the external driving field eventually destroys the vortex lattices.

5.5. Dynamics of giant vortices in rapidly rotating condensates

In this section, we study the dynamics of giant vortices in rapidly rotating two-component BECs, i.e. when Ω is large. In this case, the angular rotation leads to a large centrifugal force and the harmonic potential is not tight enough to confine all atoms. Thus, we consider a harmonic-plus-quartic potential which has the form of

$$V_j(\mathbf{x})=\alpha r^2+\kappa r^4\quad\text{with } r=\sqrt{x^2+y^2},\ j=1,2. \tag{5.10}$$

[3] See Fig. 4 in [45].
[4] See Fig. 5 in [45].

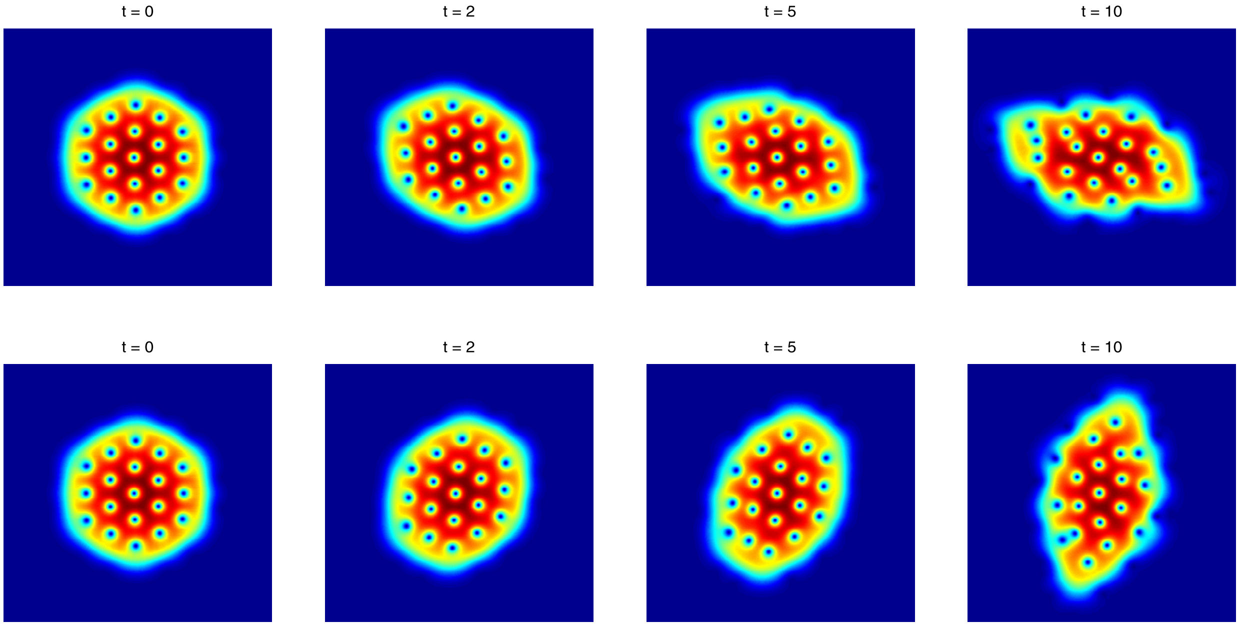

Fig. 6. Contour plots of $|\psi_1|$ (top row) and $|\psi_2|$ (bottom row) at different time for Case (i) in Section 5.4. Displayed domain $(x, y) \in [-10, 10]^2$.

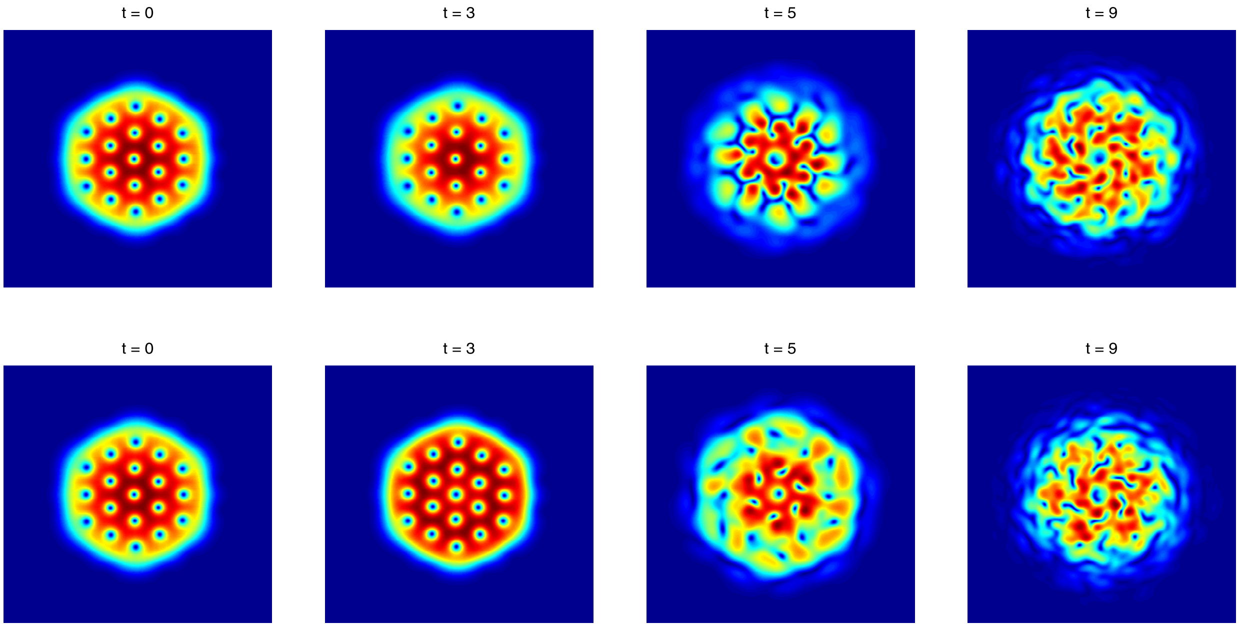

Fig. 7. Contour plots of $|\psi_1|$ (top row) and $|\psi_2|$ (bottom row) at different time for Case (ii) in Section 5.4. Displayed domain $(x, y) \in [-10, 10]^2$.

Correspondingly, the potential $W_j(\tilde{\mathbf{x}}, t)$ in (2.5)–(2.6) is time-independent and $W_j(\tilde{\mathbf{x}}, t) = V_j(\tilde{\mathbf{x}})$. The initial conditions are chosen as stationary giant vortices computed with $\Omega = 3$, $\lambda = 0$, $\alpha = -0.1$ and $\kappa = 0.2$ in (5.10) and

$$\begin{pmatrix} \beta_{11} & \beta_{12} \\ \beta_{21} & \beta_{22} \end{pmatrix} = 500 \begin{pmatrix} 1.03 & 1.0 \\ 1.0 & 0.97 \end{pmatrix}.$$

Then we study its dynamics in the following two cases: at time $t = 0$,

Case (i) Change the external potentials by setting $\kappa = 0.1$;
Case (ii) Turn on the external driving field by setting $\lambda = 0.2$.

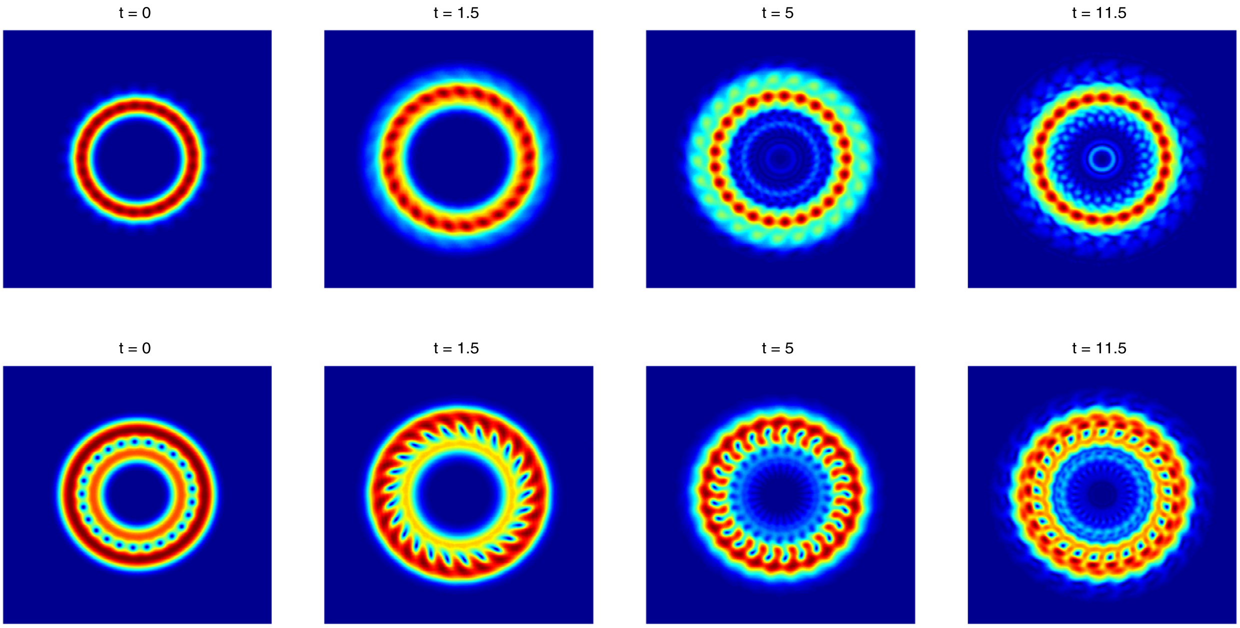

Fig. 8. Contour plots of $|\psi_1|$ (top row) and $|\psi_2|$ (bottom row) at different time for Case (i) in Section 5.5. Displayed domain $(x, y) \in [-7.5, 7.5]^2$.

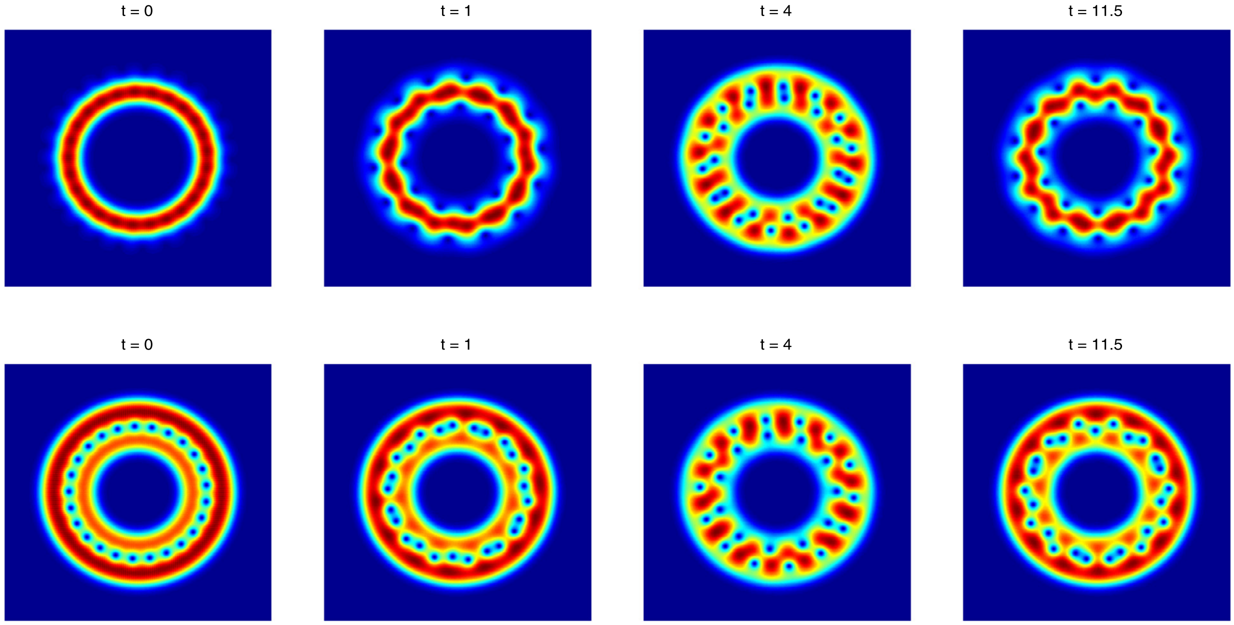

Fig. 9. Contour plots of $|\psi_1|$ (top row) and $|\psi_2|$ (bottom row) at different time for Case (ii) in Section 5.5. Displayed domain $(x, y) \in [-6, 6]^2$.

Figs. 8, 9 depict the contour plots of $|\psi_1|$ and $|\psi_2|$ at different time t in Cases (i) and (ii), respectively, where we choose the computational domain $\mathcal{D} = [-12, 12]^2$ with $h_{\tilde{x}} = h_{\tilde{y}} = \frac{3}{256}$ and the time step $k = 0.0001$. Initially, there is a giant vortex at the center of the 1st component and all atoms are squeezed into a thin annulus, while in the 2nd component the giant vortex is surrounded by many single vortices. In Fig. 8, we see that when the external potential becomes shallow (i.e. κ becomes smaller), the stationary states start rotating and expanding. After certain time, atoms enter the center and giant vortices are destroyed, but the single vortices are still remained in the 2nd component. While in Fig. 9, turning on the external driving field allows the two components to exchange their atoms and thus the giant vortices at the center of each component are relaxed and many single vortices are presented in each component. This process repeated periodically. In addition, to simulate the dynamics of giant vortices in rapidly rotating condensates, the accuracy of a numerical method is highly demanded. Our numerical simulations show that our method is very efficient in this case.

6. Summary

We proposed an efficient spectral method to solve the coupled Gross–Pitaevskii equations (CGPEs) with an angular momentum rotation term and an external driving field term, which is usually used to describe the dynamics of rotating two-component Bose–Einstein condensates (BECs) with an internal Josephson junction. We eliminated the angular momentum rotation term from the CGPEs via a rotating Lagrangian coordinate transformation, which makes it possible for developing an efficient numerical method. Then under the new coordinates, we designed a time-splitting sine pseudo-spectral method to solve the CGPEs, where a linear transformation was used to treat the external driving field term so that it does not introduce any extra computational complexity. Our method has spectral-order accuracy in space and the second-order accuracy in time. It is explicit and easy to be implemented. To demonstrate its efficiency, we compare our method with those presented in the literature. Numerical results showed that to achieve the same accuracy, the computing time spent by our method is much shorter. We then numerically examined the conservation of the angular momentum expectation and studied the dynamics of condensate widths and center of mass for different angular velocities. In addition, the dynamics of vortex lattice and giant vortices in rotating two-component BECs were studied by applying our method. Numerical studies showed that our method is very effective for studying the dynamics of rotating two-component BECs for both slowly and rapidly rotating cases.

Acknowledgements

We appreciate Prof. Weizhu Bao and Ms. Xiaomeng Cao for their fruitful discussion on the project. This work was partially supported by the Singapore A*STAR SERC Grant No. 1224504056 (Q. Tang) and the Simons Foundation Award No. 210138 and NSF Grant DMS-1217000 (Y. Zhang).

Appendix A. Calculating $\psi_j(\mathbf{x}, t_n)$ $(j = 1, 2)$ via spectral interpolation

In the following, we briefly describe the spectral interpolation for computing the wave functions $\psi_j(\mathbf{x}, t_n)$ $(j = 1, 2)$ over a set of fixed grid points in Eulerian coordinates. For simplicity of notation, we will show the interpolation in two-dimension cases. Let $\mathcal{C}$ and $\mathcal{D}$ be the bounded domain in Eulerian and rotating Lagrangian coordinates, respectively. Here we assume that $\mathbf{A}^{-1}(t)\mathcal{C} \subset \mathcal{D}$ for any time $t \geqslant 0$ and the computational domain $\mathcal{D}$ in rotating Lagrangian coordinates is large enough such that $\phi_j(\tilde{\mathbf{x}}, t_n)$ $(j = 1, 2)$ vanishes outside $\mathcal{D}$. Denote

$$\mathcal{S}_{\mathcal{C}} = \left\{(x_m, y_l) \in \mathcal{C} \;\middle|\; 0 \leqslant m \leqslant M,\ 0 \leqslant l \leqslant L\right\},$$

as the set of grid points in Eulerian coordinates and

$$\mathcal{S}_{\mathcal{D}} = \left\{(\tilde{x}_s, \tilde{y}_k) \in \mathcal{D} \;\middle|\; 0 \leqslant s \leqslant J,\ 0 \leqslant k \leqslant K\right\},$$

as the set of grid points defined in (3.20) in rotating Lagrangian coordinates. Here M, L, J and K are even positive integers.

Let $\phi^n_{j,sk}$ be the numerical approximation of $\phi_j(\tilde{x}_s, \tilde{y}_k, t_n)$. Then the discrete sine transform of $\phi_j(\tilde{x}_s, \tilde{x}_k, t_n)$ at frequencies (p, q) can be obtained from the inverse transform of (3.16), i.e.

$$\hat{\phi}^n_{j,pq} = \frac{1}{JK}\sum_{s=1}^{J-1}\sum_{k=1}^{K-1}\phi^n_{j,sk}U_{pq}(\tilde{x}_s, \tilde{y}_k), \quad (p, q) \in \mathcal{T}_{JK},\ j = 1, 2, \tag{A.1}$$

where $\mathcal{T}_{JK}$ and $U_{pq}(\tilde{\mathbf{x}})$ are defined in (3.14) and (3.15), respectively.

On the other hand, from the transform (2.4) and (3.16), we can obtain the value of $\psi_j(x_m, y_l, t_n)$ for any point $(x_m, y_l) \in \mathcal{S}_{\mathcal{C}}$ via the following interpolation:

$$\psi_j(x_m, y_l, t_n) = \phi_j(\bar{\tilde{x}}_m, \bar{\tilde{y}}_l, t_n) = \sum_{p=1}^{J-1}\sum_{q=1}^{K-1}\hat{\phi}^n_{j,pq}U_{pq}(\bar{\tilde{x}}_m, \bar{\tilde{y}}_l), \quad (m, l) \in \mathcal{T}_{ML},\ j = 1, 2, \tag{A.2}$$

where $\hat{\phi}^n_{j,pq}$ is obtained from (A.1) and at time $t = t_n$, the points $(\bar{\tilde{x}}_m, \bar{\tilde{y}}_l)$ in rotating Lagrangian coordinates are computed from

$$\begin{pmatrix}\bar{\tilde{x}}_m\\ \bar{\tilde{y}}_l\end{pmatrix} = \mathbf{A}^{-1}(t_n)\begin{pmatrix}x_m\\ y_l\end{pmatrix} = \begin{pmatrix}\cos(\Omega t_n)x_m - \sin(\Omega t_n)y_l\\ \sin(\Omega t_n)x_m + \cos(\Omega t_n)y_l\end{pmatrix}, \quad (m, l) \in \mathcal{T}_{ML}.$$

The interpolation (A.1)–(A.2) is of spectral-order accuracy. Note that the points $(\bar{\tilde{x}}_m, \bar{\tilde{y}}_l)$ $((m, l) \in \mathcal{T}_{ML})$ might be non-uniformly distributed in the computational domain $\mathcal{D}$ and thus we need to use the non-uniform fast Fourier/sine transformation [15,18,19,23,29] to compute (A.2) at cost $O(JK\ln(JK))$ (suppose $ML = O(JK)$).

References

[1] J.R. Abo-Shaeer, C. Raman, J.M. Vogels, W. Ketterle, Observation of vortex lattices in Bose–Einstein condensates, Science 292 (2001) 476–479.
[2] M.H. Anderson, J.R. Ensher, M.R. Matthews, C.E. Wieman, E.A. Cornell, Observation of Bose–Einstein condensation in a dilute atomic vapor, Science 269 (1995) 198–201.
[3] X. Antoine, C. Besse, P. Klein, Numerical solution of time-dependent nonlinear Schrödinger equations using domain truncation techniques coupled with relaxation scheme, Laser Phys. 21 (2011) 1–12.
[4] P. Antonelli, D. Marahrens, C. Sparber, On the Cauchy problem for nonlinear Schrödinger equations with rotation, Discrete Contin. Dyn. Syst., Ser. A 32 (2012) 703–715.
[5] W. Bao, Ground states and dynamics of multicomponent Bose–Einstein condensates, Multiscale Model. Simul. 2 (2004) 210–236.
[6] W. Bao, Analysis and efficient computation for the dynamics of two-component Bose–Einstein condensate, in: Contemp. Math., vol. 473, AMS, 2008, pp. 1–26.
[7] W. Bao, Y. Cai, Ground states of two-component Bose–Einstein condensates with an internal atomic Josephson junction, East Asian J. Appl. Math. 1 (2011) 49–81.
[8] W. Bao, Y. Cai, Mathematical theory and numerical methods for Bose–Einstein condensation, Kinet. Relat. Models 6 (2013) 1–135.
[9] W. Bao, Q. Du, Y. Zhang, Dynamics of rotating Bose–Einstein condensates and its efficient and accurate numerical computation, SIAM J. Appl. Math. 66 (2006) 758–786.
[10] W. Bao, H. Li, J. Shen, A generalized Laguerre–Fourier–Hermite pseudospectral method for computing the dynamics of rotating Bose–Einstein condensates, SIAM J. Sci. Comput. 31 (2009) 3685–3711.
[11] W. Bao, D. Marahens, Q. Tang, Y. Zhang, A simple and efficient numerical method for computing the dynamics of rotating Bose–Einstein condensates via rotating Lagrangian coordinates, SIAM J. Sci. Comput. (2013), http://dx.doi.org/10.1137/130911111, in press.
[12] W. Bao, Q. Tang, Z. Xu, Numerical methods and comparison for computing dark and bright solitons in the nonlinear Schrödinger equation, J. Comput. Phys. 235 (2013) 423–445.
[13] W. Bao, H. Wang, An efficient and spectrally accurate numerical method for computing dynamics of rotating Bose–Einstein condensates, J. Comput. Phys. 217 (2006) 612–626.
[14] W. Bao, Y. Zhang, Dynamics of the ground state and central vortex state in Bose–Einstein condensation, Math. Models Methods Appl. Sci. 15 (2005) 1863–1896.
[15] J.P. Boyd, A fast algorithm for Chebyshev, Fourier, and since interpolation onto an irregular grid, J. Comput. Phys. 103 (1992) 243–247.
[16] S.T. Chui, V.N. Ryzhov, E.E. Tareyeva, Phase separation and vortex states in the binary mixture of Bose–Einstein condensates, JETP 91 (2000) 1183–1189.
[17] K.B. Davis, M.O. Mewes, M.R. Andrews, N.J. van Druten, D.S. Durfee, D.M. Kurn, W. Ketterle, Bose–Einstein condensation in a gas of sodium atoms, Phys. Rev. Lett. 75 (1995) 3969–3973.
[18] A. Dutt, V. Rokhlin, Fast Fourier transforms for nonequispaced data, SIAM J. Sci. Comput. 14 (1993) 1368–1393.
[19] A. Dutt, V. Rokhlin, Fast Fourier transforms for nonequispaced data. II, Appl. Comput. Harmon. Anal. 2 (1995) 85–100.
[20] A.L. Fetter, Rotating trapped Bose–Einstein condensates, Rev. Mod. Phys. 81 (2009) 647–691.
[21] J.J. García-Ripoll, V.M. Pérez-García, V. Vekslerchik, Construction of exact solution by spatial translations in inhomogeneous nonlinear Schrödinger equations, Phys. Rev. E 64 (2001), article 056602.
[22] R. Glowinski, P. Le Tallec, Augmented Lagrangian and Operator Splitting Methods in Nonlinear Mechanics, SIAM Stud. Appl. Math., vol. 9, SIAM, Philadelphia, 1989.
[23] L. Greengard, J.Y. Lee, Accelerating the nonuniform fast Fourier transform, SIAM Rev. 46 (2004) 443–454.
[24] D.S. Hall, M.R. Matthews, J.R. Ensher, C.E. Wieman, E.A. Cornell, Dynamics of component separation in a binary mixture of Bose–Einstein condensates, Phys. Rev. Lett. 81 (1998) 1539–1542.
[25] D.M. Jezek, P. Capuzzi, H.M. Cataldo, Structure of vortices in two-component Bose–Einstein condensates, Phys. Rev. A 64 (2001), article 023605.
[26] K. Kasamatsu, M. Tsubota, M. Ueda, Vortex phase diagram in rotating two-component Bose–Einstein condensates, Phys. Rev. Lett. 91 (2003), article 150406.
[27] D. Kobyakov, V. Bychkov, E. Lundh, A. Bezett, V. Akkerman, M. Marklund, Interface dynamics of a two-component Bose–Einstein condensate driven by an external force, Phys. Rev. A 83 (2011), article 043623.
[28] L. Kong, J. Hong, J. Zhang, LOD-MS for Gross–Pitaevskii equation in Bose–Einstein condensates, Commun. Comput. Phys. 14 (2013) 219–241.
[29] J.Y. Lee, L. Greengard, The type 3 nonuniform FFT and its application, J. Comput. Phys. 206 (2005) 1–5.
[30] E.H. Lieb, R. Seiringer, Derivation of the Gross–Pitaevskii equation for rotating Bose gases, Commun. Math. Phys. 264 (2006) 505–537.
[31] T. Lin, J. Wei, Ground states of N coupled nonlinear Schrödinger equations in $\mathbb{R}^n$, $n \leqslant 3$, Commun. Math. Phys. 255 (2005) 629–653.
[32] Z. Liu, Rotating multicomponent Bose–Einstein condensates, Nonlinear Differ. Equ. Appl. 19 (2012) 49–65.
[33] K.W. Madison, F. Chevy, V. Bretin, J. Dalibard, Stationary states of a rotating Bose–Einstein condensates: Routes to vortex nucleation, Phys. Rev. Lett. 86 (2001) 4443–4446.
[34] K.W. Madison, F. Chevy, W. Wohlleben, J. Dalibard, Vortex formation in a stirred Bose–Einstein condensate, Phys. Rev. Lett. 84 (2000) 806–809.
[35] M.R. Matthews, B.P. Anderson, P.C. Haljan, D.S. Hall, C.E. Wiemann, E.A. Cornell, Vortices in a Bose–Einstein condensate, Phys. Rev. Lett. 83 (1999) 2498–2501.
[36] C.J. Myatt, E.A. Burt, R.W. Ghrist, E.A. Cornell, G.E. Wieman, Production of two overlapping Bose–Einstein condensates by sympathetic cooling, Phys. Rev. Lett. 78 (1997) 586–589.
[37] M. Sepúlveda, O. Vera, Numerical methods for a coupled nonlinear Schrödinger system, Bol. Soc. Esp. Mat. Apl. 43 (2008) 95–102.
[38] J. Shen, T. Tang, L. Wang, Spectral Methods: Algorithms, Analysis and Applications, Springer, 2011.
[39] G. Strang, On the construction and comparison of difference schemes, SIAM J. Numer. Anal. 5 (1968) 505–517.
[40] H. Wang, A time-splitting spectral method for coupled Gross–Pitaevskii equations with applications to rotating Bose–Einstein condensates, J. Comput. Appl. Math. 205 (2007) 88–104.
[41] Y.-S. Wang, B.-W. Jeng, C.-S. Chien, A two parameter continuation method for rotating two component Bose–Einstein condensation in optical lattice, Commun. Comput. Phys. 13 (2013) 442–460.
[42] H. Yoshida, Construction of higher order symplectic integrators, Phys. Lett. A 150 (1990) 262–268.
[43] Y. Zhang, Numerical study of vortex interactions in Bose–Einstein condensation, Commun. Comput. Phys. 8 (2010) 327–350.
[44] Y. Zhang, W. Bao, Dynamics of the center of mass in rotating Bose–Einstein condensates, Appl. Numer. Math. 57 (2007) 697–709.
[45] Y. Zhang, W. Bao, H. Li, Dynamics of rotating two-component Bose–Einstein condensates and its efficient computation, Physica D 234 (2007) 49–69.